The influence of Y and Nb addition on the corrosion resistance of Fe-Cr-Al-Ni model alloys exposed to oxygen-containing molten Pb

Hao Shi[a], Renate Fetzer[a], Chongchong Tang[b], Dorothée Vinga Szabó[b,c], Sabine Schlabach[b,c], Annette Heinzel[a], Alfons Weisenburger[a], Adrian Jianu[a,*], Georg Müller[a]

[a] Institute for Pulsed Power and Microwave Technology (IHM), Karlsruhe Institute of Technology (KIT), Hermann-von-Helmholtz-Platz 1, 76344 Eggenstein-Leopoldshafen, Germany

[b] Institute for Applied Materials (IAM), Karlsruhe Institute of Technology (KIT), Hermann- von-Helmholtz-Platz 1, 76344 Eggenstein-Leopoldshafen, Germany

[c] Karlsruhe Nano Micro Facility (KNMF), Karlsruhe Institute of Technology (KIT), Hermann- von-Helmholtz-Platz 1, 76344 Eggenstein-Leopoldshafen, Germany

* Corresponding author. E-mail address: adrian.jianu@kit.edu (A. Jianu); hao.shi@kit.edu (H. Shi).

Keywords: Alumina-forming austenitic (AFA) alloy; Fe-Cr-Al-Ni alloy; Molten Pb corrosion; Heavy liquid metals; Alumina scale formation; Microstructure stability.

Abstract

The corrosion behaviour of four different alumina-forming austenitic model alloys (Fe-Cr-Al-Ni based) in oxygen-containing molten Pb at 600 and 650 °C has been investigated. A thin protective oxide layer is formed on all alloys after 2000 h at 600 °C, whereas increasing the temperature to 650 °C accelerates the oxidation and promotes dissolution attack. Only one composition with minor additions of Y and Nb and low Ni concentration shows corrosion resistance at 650 °C. Y and Nb have significant positive influence on the corrosion resistance and the phase composition of the alloys.

1. Introduction

Heavy liquid metals (HLM) like Pb or Pb-Bi eutectic (LBE) are promising heat transfer fluids due to their excellent thermo-physical properties [1-3]. Applications related to the energy field like Gen-IV lead-cooled fast reactors (Gen-IV LFRs), accelerator driven systems (ADS), concentrated solar power (CSP), or liquid metal batteries are considered [4-8]. However, structural steels (ferritic-martensitic (F/M) steels, stainless steels) have compatibility issues, in particularly corrosion, when they are in contact with HLMs at temperatures above 500 °C [9-14]. The corrosion of steels in HLMs is due to the dissolving of various constituents of these materials by the liquid metal (solubility in Pb: Ni>Cr>Fe) [1, 15]. The way in which this dissolution proceeds promotes different types of attack, ranging from simple dissolution-type attack to deep inter-granular attack with preferential leaching of one constituent [10, 13, 14, 16]. Besides, ferritic/martensitic steels (e.g. T91, HT9, FeCrAl alloy) are susceptible to liquid metal embrittlement (LME) at around 350 °C []. Therefore, new structural materials with excellent compatibility properties are urgent for the liquid metal applications.

Alumina forming austenitic (AFA) steels, initially developed as structural materials for energy related applications, have shown excellent corrosion resistance and mechanical properties [17-21]. By alloying with low amount of Al (<5 wt.%), AFA steels are able to form an external alumina scale in oxidizing environments at 600-900 °C [17-18]. The amount of Ni added has to balance with Al and Cr contents in order to maintain the austenitic matrix (face-centered cubic structure, f.c.c.). In addition,

small amounts of other elements can also be added to optimize the properties (e.g. mechanical, corrosion resistance, structure stability) for applications, for instance, stabilize the austenite structure (C, Cu, Mn), precipitate the minor secondary phases (Nb, Ti), increase scale adherence (Y), strengthen the austenite (W, Mo) and its grain boundaries (B) [17-29].

Recent research results indicate that alumina forming austenitic (AFA) model alloys with the chemical composition formula Fe-(20-29)Ni-(15.2-16.5)Cr-(2.3-4.3)Al (wt.%) are able to form alumina-rich protective scale during exposure to oxygen-containing molten Pb at 550-600 °C for 1000 h and to preserve the austenitic matrix [9-10]. The passive and continuous oxide scales, grown on alloy surfaces, are based on two corundum-type crystalline structures, Cr_2O_3 and Al_2O_3-Cr_2O_3 solid solutions. Besides, a transitional layer with a thickness up to 2 μm, enriched in Ni and Fe, and with randomly distributed B2-(Ni,Fe)Al precipitates is observed below the oxide scale. Underneath the transitional layer, the microstructure of the corrosion resistant AFA alloys consists of an austenitic matrix, in which Ni_3(Al, Fe) precipitates are distributed. However, (i) the oxide scale stability during longer time exposure (>2000 h), (ii) the influence of minor alloying elements on the oxide scale formation and on the microstructure stability of AFA model alloys, and (iii) the corrosion behaviour of AFA alloys at temperature above 600 °C need to be evaluated in order to qualify such alloys for applications.

The motivation of our work is to develop AFA steels targeting for energy related applications in molten Pb environment. The results shown in this paper represent the second step of our endeavor to produce real AFA steels. We evaluate the influence of minor additions of yttrium (Y), aimed at improving oxide scale adherence/stability, and of niobium (Nb), targeting precipitation hardening, on the AFA model alloys corrosion resistance. We have investigated the corrosion behaviour of Fe-Cr-Al-Ni-(Y,Nb) model alloys during exposure at temperatures ≥ 600 °C and for times ≥ 2000 h by different characterization methods X-ray diffraction and scanning electron microscopy. Moreover, the detailed investigations regarding protective oxide scale and phase compositions of alloy matrix are also performed on exposed samples.

Finally, transmission electron microscopy characterization is employed to investigate in detail the oxide scale microstructure and phase compositions of alloy matrix after corrosion test.

2. Materials and methods

Following the previous promising corrosion test results of Fe-Cr-Al-Ni based AFA model alloys in molten Pb [9], alloy H54 with 24 wt.% Ni and alloy H56 with 28 wt.% Ni were selected for this research work. To investigate the influence of minor elements addition on the corrosion behaviour and microstructure evaluation of AFA alloys when exposed to molten Pb, two new alloys H54[NbY] and H56[NbY] with minor Nb and Y addition were prepared. Table 1 shows the nominal composition of all prepared alloys.

All alloys were produced by arc melting of a mixture of the pure metal elements (purity>99.99%) in argon atmosphere. In order to facilitate composition homogenization, the ingots were flipped over and re-melted at least 5 times in a water-chilled copper mold. Then the as cast alloys were sealed in

quartz tubes with argon atmosphere for composition homogenization treatment. The samples were annealed at 1250 °C for 2 hours, followed by water quenching.

The corrosion tests were performed in stagnant molten Pb with 10^{-6} wt.% oxygen concentration in the COSTA facility (**CO**rrosion test stand for **ST**agnant liquid **A**lloys). Detailed information regarding the corrosion experiment and oxygen control system can be found in the references [9, 10, 30]. One set of samples was exposed to 600 °C for 2000 h, and the other set was exposed to 650 °C for 3550 h, respectively, as shown in Table 1. The size of each sample was around 10 mm in diameter and 1.5 mm in thickness. A hole with diameter of 1.5 mm was drilled in each sample to hang and fasten the sample with a Mo-wire when immersing the sample into molten Pb. All of the samples were grounded with a 1200 grit surface finish sandpaper. Then, the specimens were cleaned by distilled water, acetone and ethanol in an ultrasonic bath before the corrosion test. The oxygen content in the molten Pb was controlled by adjusting the oxygen partial pressure in the adjacent gas phase. A dedicated glove-box conditioned to the similar oxygen partial pressure as in the furnace was used to introduce the samples. When the glove box connected to the furnace, the alumina crucibles containing the pre-conditioned molten Pb were transferred into the glove box. Then, all samples were fully immersed into the molten Pb and the crucibles were put back into the furnace as fast as possible.

Table 1
Corrosion test parameters of AFA samples in 10^{-6} wt.% oxygen containing molten Pb.

Code	Nominal composition (wt.%)	Corrosion test conditions	
H54	Fe-16Cr-4Al-24Ni	600 °C/2000 h	650 °C/3550 h
H56	Fe-15Cr-3.5Al-28Ni	600 °C/2000 h	650 °C/3550 h
H54^{NbY}	Fe-16Cr-4Al-24Ni-1.5Nb-0.5Y	600 °C/2000 h	650 °C/3550 h
H56^{NbY}	Fe-15Cr-4Al-28Ni-1.5Nb-0.5Y	600 °C/2000 h	650 °C/3550 h

After the corrosion exposure, samples were extracted from molten Pb using the same glove-box conditioned to the same way as for the loading process. A simple visual check of exposed samples found that the samples' surfaces were almost Pb free or with only a few small areas covered by Pb layer. Then the remaining adherent Pb was cleaned by immersing the samples into a solution of ethanol, acetic acid and hydrogen peroxide (1:1:1) for 15 min. The cleaning method is accepted as a standard procedure, which does not degrade the oxide scale or the alloys [31].

The phase composition of all samples and conditions was analyzed by X-Ray Diffraction (XRD, Seifert PAD II) with Cu $K_{\alpha1}$ radiation (λ=0.15406 nm, 40 kV and 30 mA) in Bragg–Brentano geometry (θ-2θ) with a step size of 0.02° and a scan speed of 0.1 °/min.

Before and after corrosion test, the microstructure of all samples was characterized by Scanning Electron Microscopy (SEM, model: Philips XL 40 SEM with LaB$_6$ cathode, or Hitachi S-4800 with cold field emission electron source), both equipped with an Energy Dispersive X-Ray Spectrometer (EDS).

In SEM, a focused electron beam with energy of 20 keV and working distance of 10 mm interacts with the sample in a teardrop-shape (around 0.1-5 μm deep into the sample) [32]. The sample surface was directly characterized by SEM/EDS without further preparation. For SEM/EDS cross section analysis, an electroplated nickel layer with ~40 μm thickness was deposited to protect the surface oxide scale from detachment during sample preparation. Then the sample was fixed and embedded with resin. All embedded samples were ground by 1200# and 2400# grid sand paper, polished with diamond paste (1 μm diameter diamond particles), and sputtered with a thin, electrically conducting layer of gold.

In addition, the oxide scale structure of H54 and H54^{NbY} after 2000 h exposure at 600 °C was evaluated by Transmission Electron Microscopy (TEM). TEM lamellae were prepared by a Dual beam Focused Ion Beam (FIB-SEM) technique (FEI Strata 400S Dual beam FIB equipped with Omniprobe™ 200 micromanipulator). To protect the target area from the ion impact, a Pt layer was deposited beforehand. The lamellae were analyzed by a TEM (FEI Tecnai G² F20 ST), operated at 200 keV with a field emission gun, equipped with an Orius SC600 CCD Camera (Ametek, Pleasantron, California, USA), and a S-UTW EDS Si(Li) Detector (EDAX, Mahwah, New Jersey, USA) for elemental analysis, and a HAADF-detector for STEM-mode.

3. Results

3.1 Phase composition

The XRD spectra of the AFA alloys before and after corrosion tests are shown in Fig. 1. According to the patterns depicted in Fig.1 (a), the microstructure of the annealed AFA alloys consists only of a single-phase, the f.c.c. austenite phase. No other metallic phases or oxides are detected.

After 2000 h exposure at 600 °C to oxygen containing molten Pb, beside austenite as the dominant phase, additional metallic and oxidic phases have developed within/on the alloys, as shown in Fig. 1 (b) and summerized in Table 2. As metallic phases, two body-centered cubic (b.c.c.) structures, the B2-type ordered intermetallic compound NiAl and the solid solution Fe-Cr (ferrite) are identified in the XRD patterns of some samples, cf. Table 2. B2 phase has the main peaks approaching to that of ferrite at position of (110), (200) and (211), while an additional main peak is only existed for B2 at (100). These metallic phases are formed within the bulk alloys. The oxide phases, corumdum corundum-type Cr_2O_3 and the spinel-type phases Fe_3O_4 and $Fe(Cr,Al)_2O_4$, identified based on their major peaks, are assumed to have grown on the samples surface. Moreover, the peak observed at around 2θ=38° in the XRD patterns of H54, H56, and H54^{NbY} could indicate the presence of the third oxide phase, $(Al,Cr)_2O_3$ with corundum structure [9]. This hypothesis will be confirmed within this paper by the SEM and TEM investigation results.

The XRD patterns of the samples exposed at 650 °C for 3550 h to oxygen-containing molten lead, displayed in Fig. 1 (c) and summarized in Table 2, contain the characteristic peaks of the same metallic phases observed after corrosion tests performed at 600°C: the f.c.c. austenite, B2-NiAl and b.c.c. ferrite. However, the austenite phase is the dominant phase only in case of H54^{NbY}, while ferrite becomes the dominant phase within the other three alloys, H54, H56, and H56^{NbY}. It is judged by the

related weak intensity from austenite while the intensity from ferrite is quite strong. In addition, the peaks corresponding to the oxides (Cr_2O_3, Fe_3O_4, $(Al,Cr)_2O_3$) are clearly present on the H54[NbY] and barely visible on the other samples made of H54, H56, and H56[NbY]. The lack of the protective oxides, the decrease of the austenite amount, and the significant increase in the amount of ferrite, are indications that the samples H54, H56, and H56[NbY] have suffered from corrosive attack with preferential leaching of Ni. Such dissolution attack leads to phase transformation and recrystallization in the affected volume.

a)   b)   c)
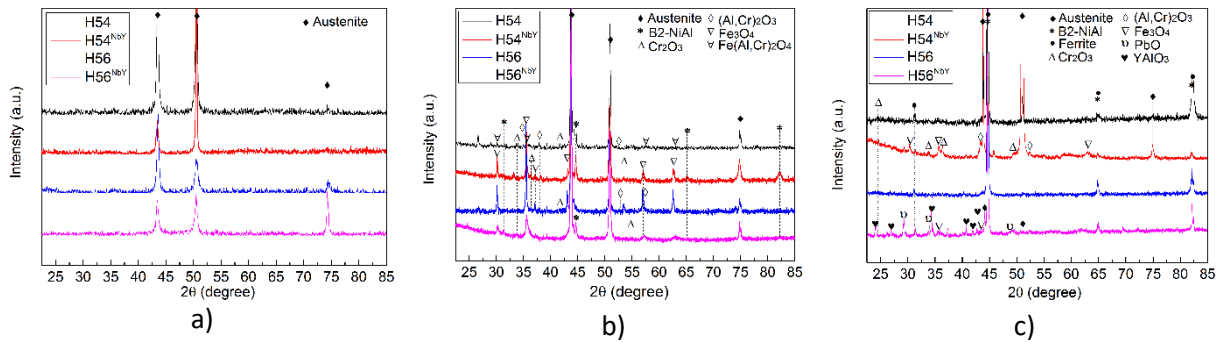
Fig. 1. XRD spectra of the AFA alloys H54, H56, H54[NbY], and H56[NbY] in the different conditions: a) after 2 h annealing treatment at 1250 °C, b) after 2000 h corrosion test in Pb at 600 °C, c) after 3550 h in Pb at 650 °C.

Table 2
Phase composition of H54, H56, H54[NbY], and H56[NbY] after corrosion test in Pb for 2000 h at 600 °C and for 3550 h at 650 °C, respectively, measured by XRD.

Sample	Temp. (°C)	Phase composition[1] Cr_2O_3 (74-326)	$(Al,Cr)_2O_3$ (77-2188)	$Fe(Cr,Al)_2O_4$ (3-873)	Fe_3O_4 (79-418)	Austenite (33-397)	B2-NiAl (44-1187)	Fe-Cr (ferrite) (34-396)	Other
H54	600	+	+	+	+	+	+	-	
	650	-	-	-	-	+ (weak)	+	+ (strong)	
H56	600	+	+	+	+	+	-	-	
	650	-	-	-	-	-	+	+ (strong)	
H54[NbY]	600	+	+	-	+	+	+	+	
	650	+	-	-	+	+	+	-	
H56[NbY]	600	+	-	-	+	+	+	-	
	650	-	-	-	+	+ (weak)	+	+ (strong)	PbO, $YAlO_3$

[1] PDF no. is given in brackets.

3.2 Microstructure

Before the corrosion experiments, the microstructure of all samples has been characterized by SEM. The alloys H54 and H56 display the same type of morphology, namely a homogenous morphology and large grains with the size in the range 0.3-2 mm. Fig. 2 (a) shows as example the microstructure of H54. Alloys H54[NbY] and H56[NbY] exhibit a microstructure similar with the basic alloys H54/H56. The difference consists in the presence of randomly distributed Al-Ni-Y-rich precipitates,

appearing as bright precipitates (Fig. 2 (b)). This is an effect of Y over-doping. Although Y-rich precipitates are visible by SEM, they could not be identified by XRD due to their low fraction (< 5 %) in the alloy matrix.
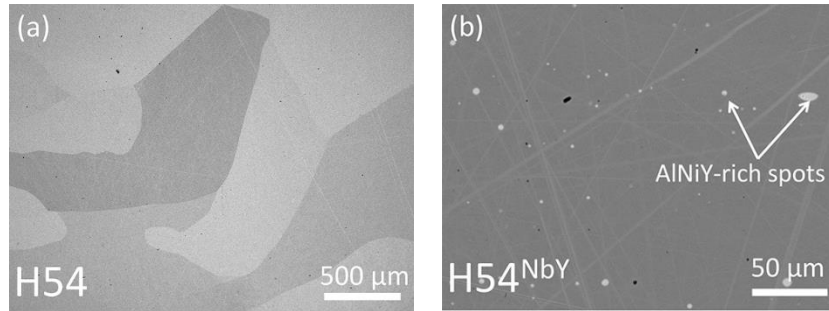
Fig. 2. Representative SEM micrographs of annealed AFA alloys, (a) H54; (b) H54^{NbY}.

The chemical compositions of all AFA alloys measured by EDS are shown in Table 3.

Table 3
Chemical compositions of AFA alloys (wt.%), measured by EDS.

Sample	Nominal composition (wt.%)	Cr	Al	Ni	Nb	Y	Fe
H54	Fe-16Cr-4Al-24Ni	16.3	4.3	23.4	-	-	Bal.
H56	Fe-15Cr-3.5Al-28Ni	15.2	3.8	28.5	-	-	Bal.
H54^{NbY}	Fe-16Cr-4Al-24Ni-1.5Nb-0.5Y	16.6	4.3	22.9	1.2	0.3	Bal.
H56^{NbY}	Fe-15Cr-4Al-28Ni-1.5Nb-0.5Y	15.5	4.2	28.0	1.1	0.3	Bal.

Fig. 3 shows SEM images of the microstructure of bulk alloys of H54 and H54^{NbY} after the corrosion tests at 600 °C and 650 °C, respectively. The image of bulk alloy has been taken from the center of the polished cross section. According to Fig. 3 (a), (b), the alloy matrix of H54 shows a homogeneous morphology after 2000 h exposure at 600 °C, while H54^{NbY} exhibit very fine grains fine precipitates with dark contrast. The B2-NiAl and ferrite phases identified by XRD (see Fig. 1 (b) and Table 2) are attributed to these fine precipitates, later confirmed by TEM results. However, in case of H54 these phases are not visible in the bulk alloy by SEM. This might either be due to the limited contrast of the SEM image or because the second phases/precipitates form mainly near the exposed surface (the location where XRD analysis was performed) and not in the bulk alloy of H54.

Fig. 3 (c), (d) show representative SEM images of H54 and H54^{NbY} exposed to 650 °C for 3550 h. The rod-shaped precipitates, homogeneously distributed over the entire alloy matrix of H54 (Fig. 3 (c)), show an enrichment of Ni and Al (SEM/EDS). They are attributed to the B2-NiAl phase identified by XRD. Besides, some of the dark contrast, strip-like Ni-Al-rich precipitates are accompanied by bright Fe-Nb-rich particles in the alloy matrix of H54^{NbY} (Fig. 3 (d)).
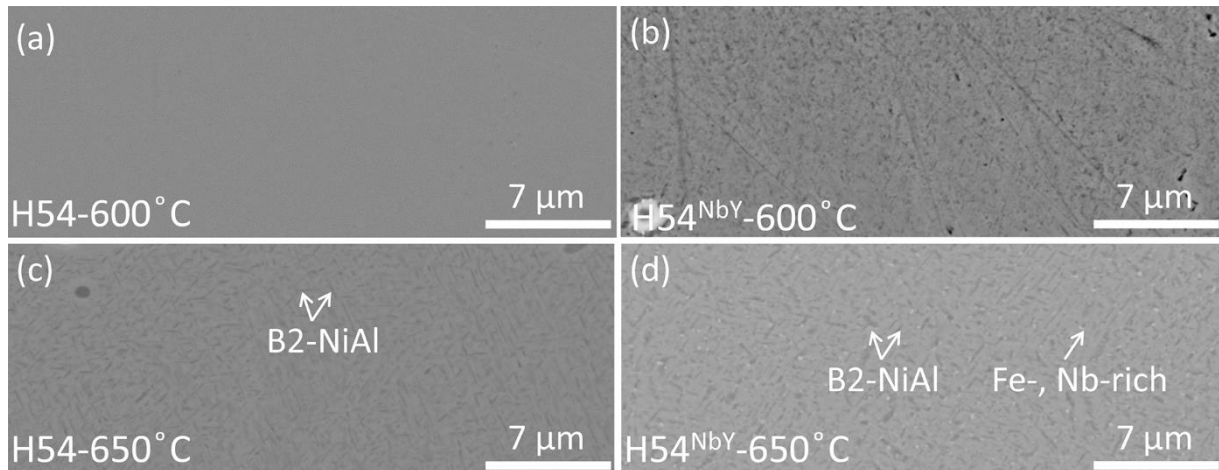
Fig. 3. Microstructure in alloy matrix after exposed to 10^{-6} wt.% oxygen-containing molten Pb, (a) H54 with 2000 h exposure at 600 °C; (b) H54^{NbY} with 2000 h exposure at 600 °C; (c) H54 with 3550 h exposure at 650 °C; (d) H54^{NbY} with 3550 h exposure at 650 °C.

3.3 SEM evaluation
3.3.1 Surface

At 600 °C, all AFA alloys have proven their corrosion resistance to 10^{-6} wt.% oxygen-containing molten Pb after 2000 h exposure. Fig. 4 presents the surface morphology of all AFA alloys after the corrosion test. A continuous, protective oxide scale covers all alloy surfaces. There is no evidence of corrosion attack for any of the investigated alloys. H54 shows the formation of a continuous oxide scale featured with some Al-Cr-rich spots in dark-gray contrast (around 20% of the surface area), as measured by EDS. Concurrent with the XRD results, these regions might be attributed to Fe(Cr,Al)$_2$O$_4$ spinel-type oxide, see also the cross section analysis below. Compared with H54, the surface of H56 shows smaller and less Fe(Cr,Al)$_2$O$_4$ dark-gray spots (<2% surface area). In addition, however, Fe-rich oxide protrusions (around 5% of the surface area) are observed and identified by EDS analysis, which are identified as magnetite in agreement with the XRD results. The dark-gray spots of Fe(Cr,Al)$_2$O$_4$, which are visible on the Y-free alloys H54 and H56, cannot be observed on the Nb-Y-containing samples H54^{NbY} and H56^{NbY}. However, magnetite protrusions are grown also on the surfaces of both H54^{NbY} and H56^{NbY}. They are smaller than that observed on H56 and also account for around 5% of the surface area.
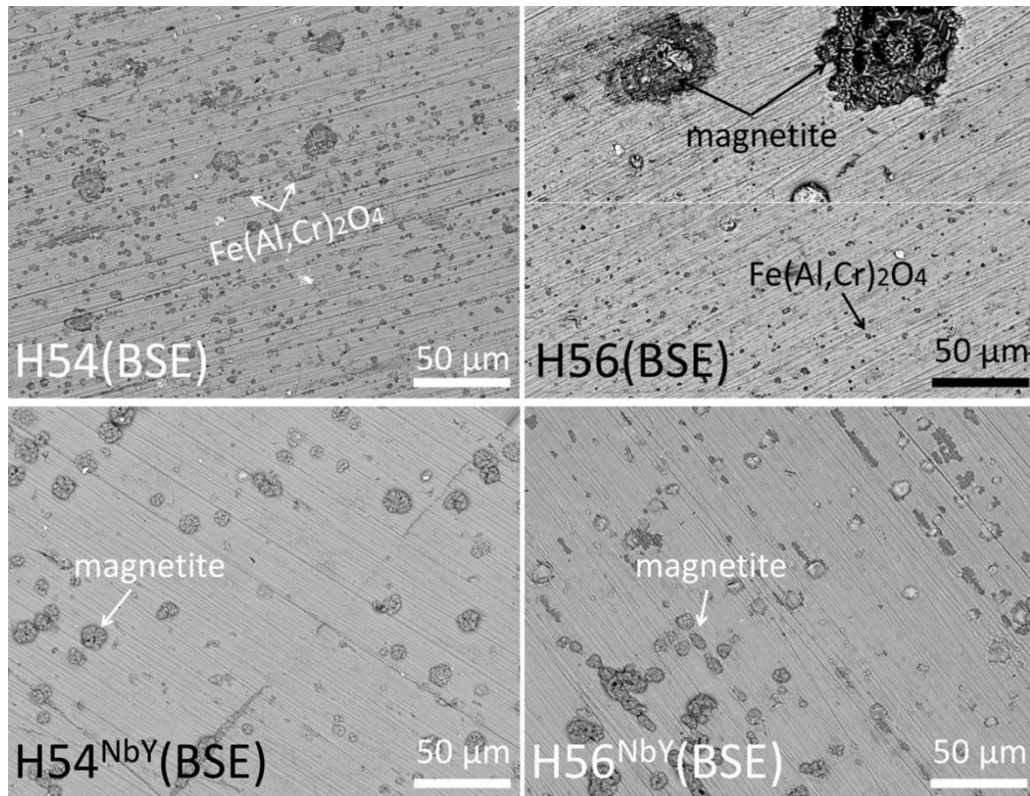
Fig. 4. SEM surface morphologies of AFA model alloys (H54, H56, H54^{NbY} and H56^{NbY}) after 2000 h exposure to 10^{-6} wt.% oxygen-containing molten Pb at 600 °C, acquired with backscattered electrons (BSE).

At 650 °C, alloys H54, H56 and H56^{NbY} show dissolution attack in some areas, while H54^{NbY} remains protected by a continuous oxide scale. This is shown in Fig. 5. The alloys H54, H56, and H56^{NbY} show the evidence of oxide scale formation at some areas. However, pores in the oxide scale and dissolution attack are found in many regions, especially H56 exhibits more than half of the surface area attacked. This is in agreement with the XRD results showing weak (H54, H56^{NbY}) or no (H56) signals from the austenitic phase but strong signals from the ferritic (b.c.c.) phase due to phase transformation (f.c.c. → b.c.c.) triggered by preferential leaching of Ni. In contrast, H54^{NbY} is the only alloy that has formed a protective oxide scale after 3550 h at 650 °C, with a few Fe-rich oxide protrusions. No evidence of dissolution attack is observed on this alloy.
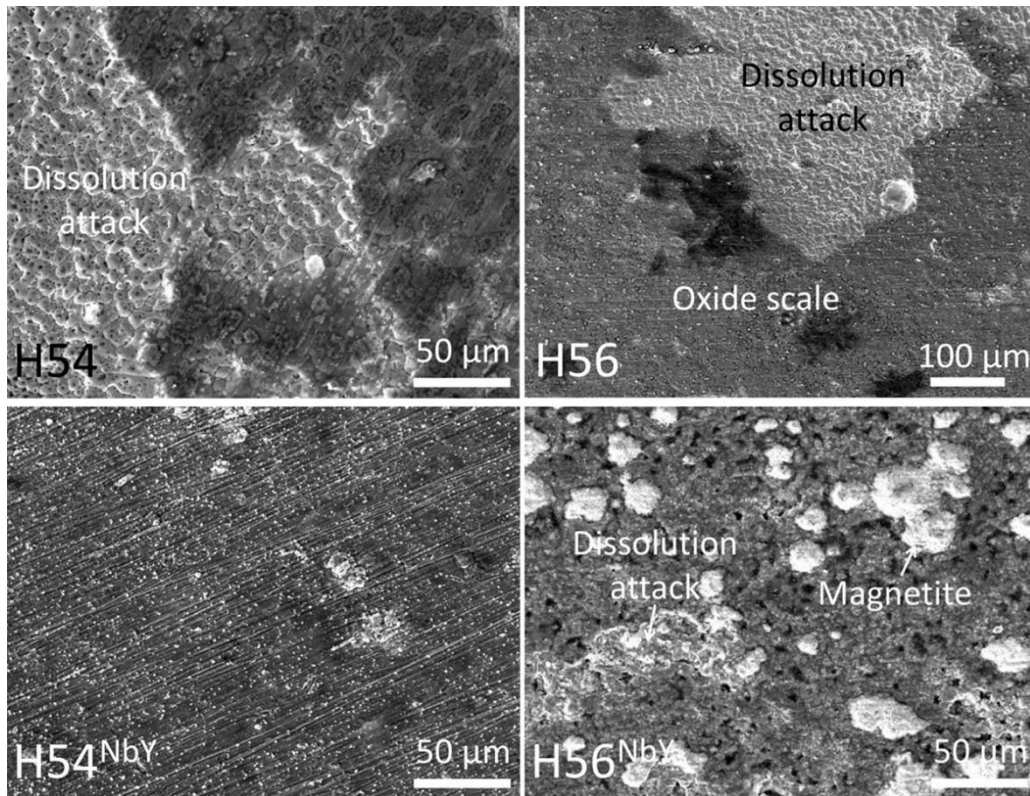
Fig. 5. SEM surface morphologies of AFA model alloys (H54, H56, H54^{NbY} and H56^{NbY}) after 3550 h exposure to 10^{-6} wt.% oxygen-containing molten Pb at 650 °C.

3.3.2 Cross section

To investigate the corrosion behaviour and scale formation in more detail, SEM/EDS cross section analysis was performed. The results for the most promising alloy, namely H54^{NbY}, are presented in comparison to the alloy H54. Only H54^{NbY} shows corrosion resistance at 650 °C, while all other samples suffer from corrosion attack under these conditions.

Fig. 6 shows an example of the EDS element mapping of the cross section of alloy H54 after 2000 h exposure at 600 °C. A continuous oxide scale covers the surface. Neither dissolution attack nor Pb penetration underneath the oxide layer can be observed. Some Al-rich and Cr-rich spots are visible below the oxide scale of H54. Concurrent with the XRD results, the Al-rich precipitates are attributed to the identified B2-NiAl phase.
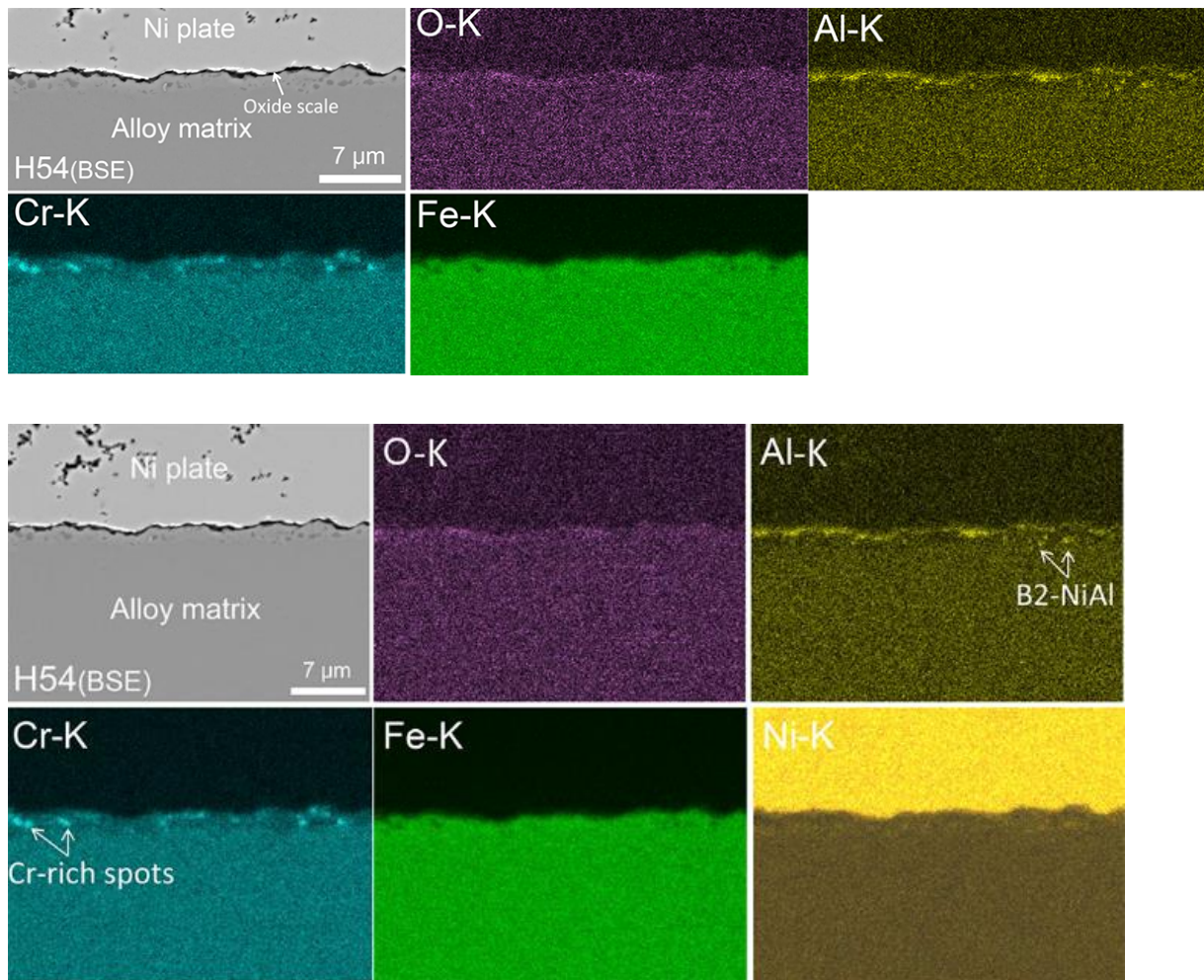
Fig. 6. SEM cross section image and EDS mapping of H54 after 2000 h exposure to 10^{-6} wt.% oxygen-containing molten Pb at 600 °C.

Fig. 7 shows an EDS line scan of the cross section of H54 after 2000 h exposure at 600 °C. The maximum signal of O-K coincides with maxima of Al-K and Cr-K signals in the oxide layer region, indicating the formation of an Al-Cr-based oxide layer. This is in agreement with the XRD results, where the corundum-type oxides Cr_2O_3 and $(Al,Cr)_2O_3$ were identified. Since the oxide scale is very thin (< 200 nm), it is difficult to directly measure its thickness from the SEM image. The dark-gray $Fe(Cr,Al)_2O_4$ spots already observed on the surface of H54 and H56 (Fig. 4) are thicker (>0.7 µm) than the general oxide layer. EDS measurements of these thick areas (e.g. the Al-Cr-rich oxide spot in Fig. 7) reveal concentrations of O, Cr, Al and Fe consistent with $Fe(Cr,Al)_2O_4$ spinel-type, an oxide phase also identified by XRD.

Below the general oxide scale, a bright layer, which shows a slight depletion in Al and Cr but enrichment in Fe and Ni, called transitional layer (TL) [9], is observed for H54. The thickness of this layer varies from 0.5 to 2 µm. Some dark precipitates are visible in the TL. The EDS line scan confirms the results from elemental mapping (Fig. 6) that these precipitates are enriched in Ni and Al and represent the B2-NiAl phase identified by XRD. Neither Al-Ni-rich precipitates nor Cr-rich spots are observed in the bulk alloy below the transitional layer.
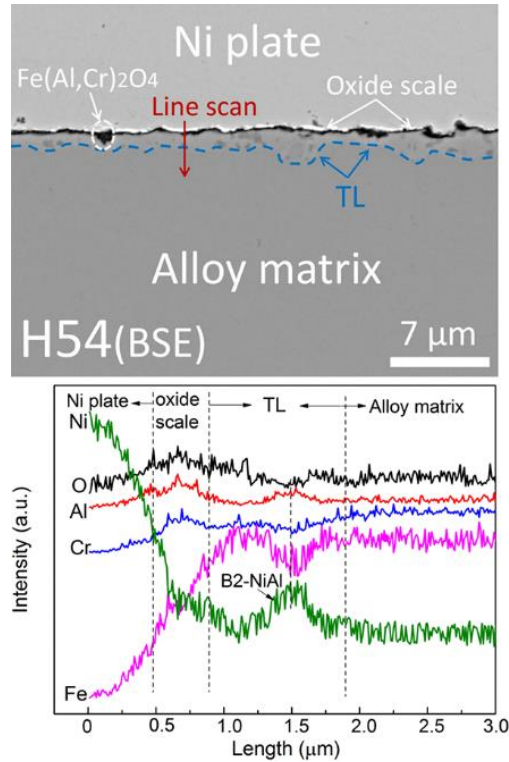
Fig. 7. SEM cross-section and EDS line scan of the cross section of H54 after 2000 h exposure to 10^{-6} wt.% oxygen-containing molten Pb at 600 °C, TL: transitional layer.

Fig. 8 shows the EDS elemental maps in the cross section of H54^{NbY} after 2000 h exposure at 600 °C. A uniform and thin oxide scale is observed, which mainly consists of O and Al. These elements are distributed uniformly in the oxide scale region. Neither dissolution attack nor Pb penetration is observed. Fig. 9 presents a typical line scan of the cross section of the alloy H54^{NbY}. It indicates that the maximum signal of O-K roughly coincides with maxima of Al-K and Cr-K signals in the oxide layer region. This indicates, as in case of H54, an Al-Cr-based oxide scale, which is in agreement with the oxides Cr_2O_3 and $(Al,Cr)_2O_3$ identified by XRD. Due to limited resolution, no further information about the composition and microstructure of the oxide scale can be gained. Below the oxide scale, a transitional layer is identified, see Fig. 9. The thickness of the transitional layer is in the range of 0.5 to 1 μm, which is thinner than that formed on H54 for the same exposure time. Within the TL, precipitates in dark and bright contrasts are observed. According to EDS analysis, the dark areas represent an Al-Ni-rich phase, the B2-NiAl phase identified by XRD. The bright precipitates, which are in close proximity to the dark precipitates, are rich in Fe and Nb, which may indicate the formation of Fe_2Nb Laves phase.
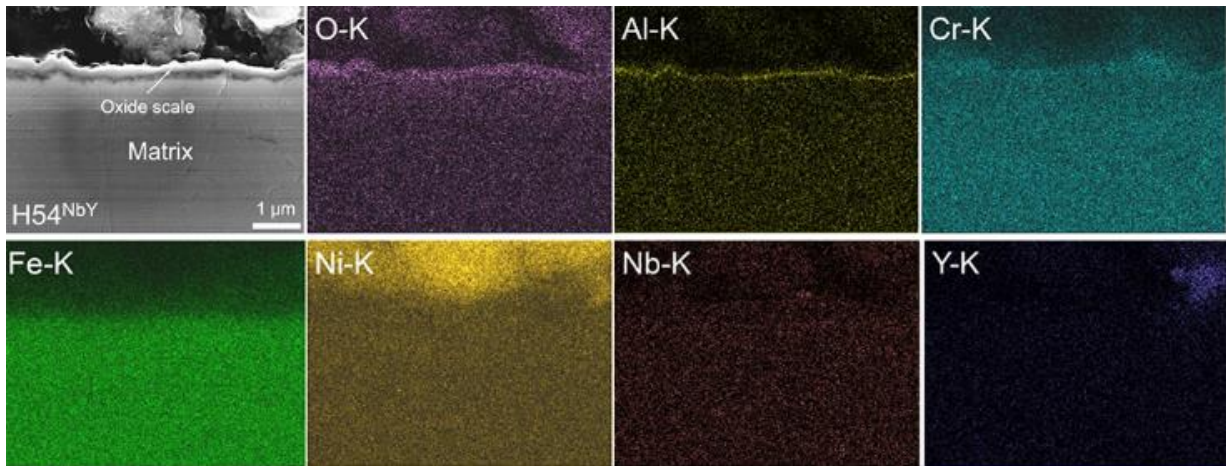
Fig. 8. SEM cross section image and EDS mapping of H54^{NbY} after 2000 h exposure to 10^{-6} wt.% oxygen-containing molten Pb at 600 °C.
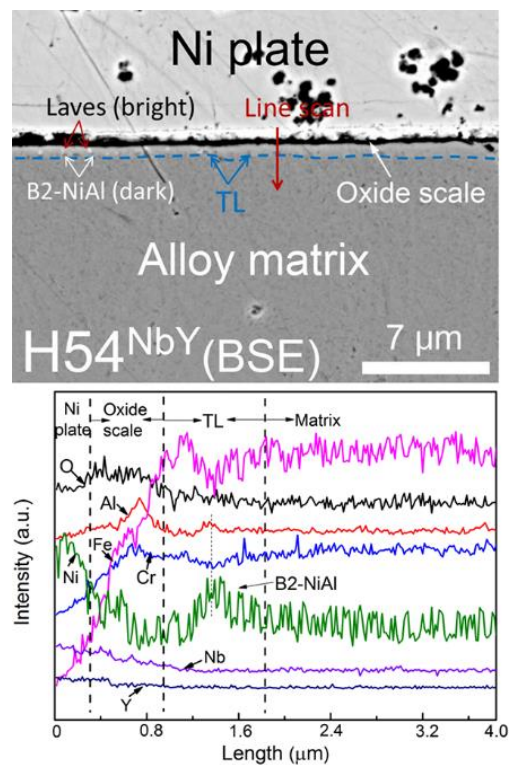
Fig. 9. SEM cross-section and EDS line scan of the cross section of H54^{NbY} after 2000 h exposure to 10^{-6} wt.% oxygen-containing molten Pb at 600 °C, TL: transitional layer.

Figs. 10 and 11 show examples of the cross section analysis of H54 and H54^{NbY}, respectively, after 3550 h exposure at 650 °C. According to the EDS cross section element mapping of H54 (Fig. 10), parts of the alloy surface are covered by Al-Cr-rich oxide scale while in other areas dissolution attack is observed. There is a clear depletion in Ni and an enrichment in Fe observed close to the surface. In contrast to the dissolution attack observed in some regions of the alloy H54, a continuous protective oxide scale covers the alloy surface of H54^{NbY} (see Fig. 11). EDS element mapping shows that the oxide scale mainly consists of O and Al, and both elements are distributed uniformly in the

12

layer. According to the line scan measurement (Fig. 12), the oxide scale with the thickness around 350 nm is rich in Al and Cr, with the maximum of the Cr signal located at the outer part of the scale and the maximum of the Al signal detected at the inner part of the scale. Below the oxide scale, there is a slight depletion of Al and a clear enrichment of Ni in the transitional layer (TL), which has a depth of up to 4 µm. Both the B2-NiAl precipitates (dark spots) and the Nb-rich spots (bright, possibly Laves phase), clearly visible and homogeneously distributed over the entire bulk alloy, experience a coarsening in the TL: their number and the contrast between precipitates and matrix in the SEM (BSE) image decreases, whereas their size increases.
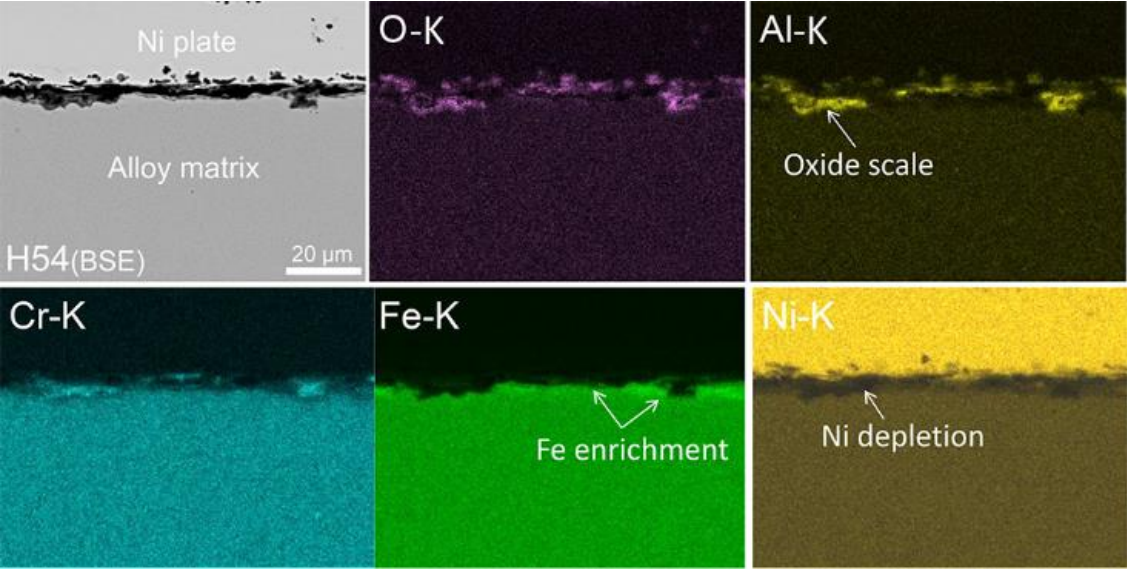
Fig. 10. EDS mapping of the cross section of H54 after 3550 h exposure to 10^{-6} wt.% oxygen-containing molten Pb at 650 °C.
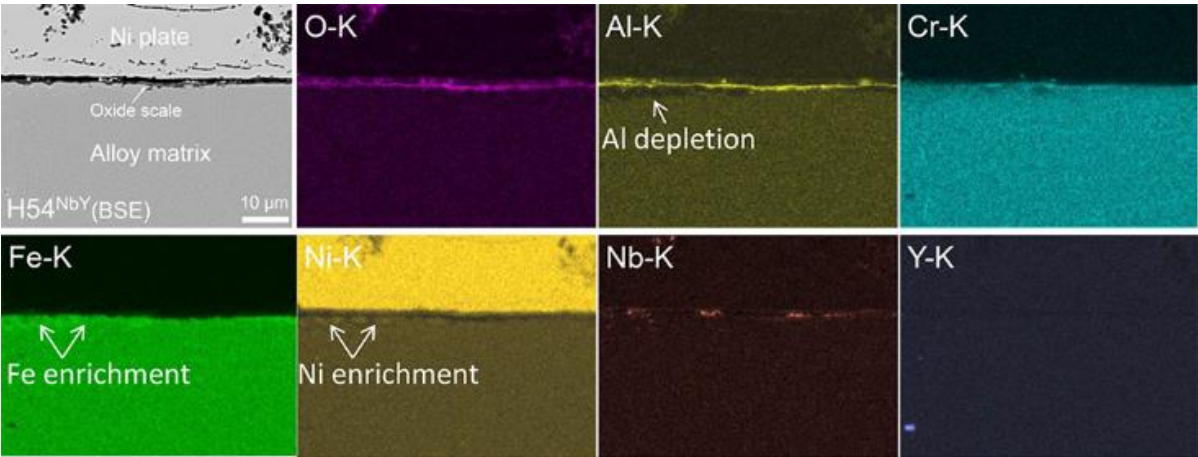
Fig. 11. EDS mapping of the cross section of H54^{NbY} after 3550 h exposure to 10^{-6} wt.% oxygen-containing molten Pb at 650 °C.
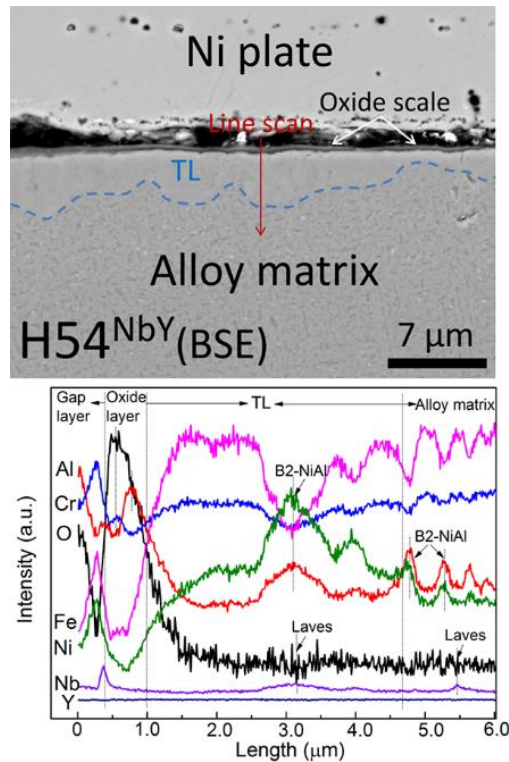
Fig. 12. SEM cross-section and EDS line scan of the cross section of H54^{NbY} after 3550 h exposure to 10^{-6} wt.% oxygen-containing molten Pb at 650 °C, TL: transitional layer.

3.4 TEM evaluation

By XRD and SEM, it was possible to investigate the general corrosion behaviour of AFA alloys exposed to oxygen-containing molten Pb. However, it is difficult to characterize the microstructure of the thin oxide layers (< 200 nm) and small size precipitates in the alloy matrix and transitional layer. Thus, TEM characterization is applied to analyze the promising alloys H54 and H54^{NbY} after 2000 h exposure to 600 °C in more detail, as they behave excellent in oxygen-containing molten Pb.

3.4.1 Alloy H54

Fig. 13 shows the TEM results obtained by imaging with different magnifications and performing selected area electron diffraction (SAED) of different representative areas. Fig. 13 (a) shows an overview bright-field (BF) image of the FIB-lamella at low magnification. The thin oxide scale is highlighted with an arrow. The diffraction pattern of the alloy matrix (marked as circle in Fig. 13 (a)) confirms the austenitic (f.c.c.) nature of the matrix, see Fig. 13 (b), and is in agreement with XRD-results (see Fig. 1 (b) and Table 2). The zone axis parallel to the electron beam is close to [001]. The highlighted spots can be attributed to (-200), (020), and (-220), respectively. Fig. 13 (c) shows the oxide scale at higher magnification. The Pt is the protecting layer stemming from the FIB-process. SAED from the oxide scale (Fig. 13 (d)) shows a ring pattern, which indicates the formation of nano-crystalline oxides. This result is further approved by high-resolution TEM image in Fig. 13 (e). Small grains can be seen, and lattice fringes with a spacing of 0.19 nm, attributed to (202) planes of corundum, are identified from the image. Based on the measured spacing, the ring pattern also belongs to a corundum type phase (Al$_x$Cr$_{1-x}$)$_2$O$_3$, with x=0.85-0.9. The measured thickness of the oxide scale is around 50 nm.
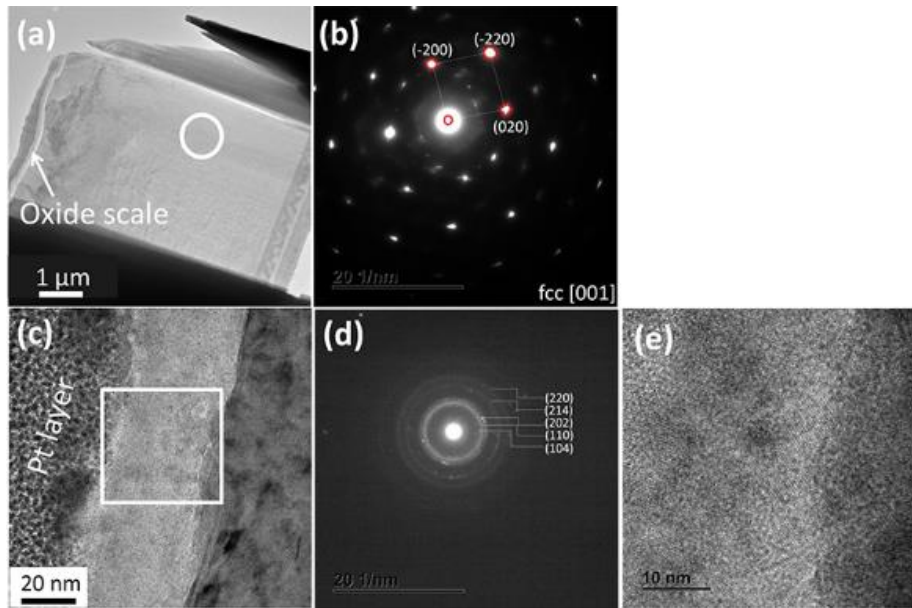
Fig. 13. TEM characterization of H54 after 2000 h exposure to 10^{-6} wt.% oxygen-containing molten Pb at 600 °C. (a) BF overview image, (b) corresponding SAED obtained on bulk alloy, (c) BF image of the oxide scale, (d) corresponding SAED of the oxide scale, (e) high resolution image of the oxide scale.

In addition, chemical compositions within the oxide layer have been measured by HAADF-STEM STEM-EDS. Table 4 summarizes the standardless quantitative results of elemental concentrations from the two regions (Reg-1 and Reg-2) shown in Fig. 14, quantified with absorption correction for the thin oxide layer. According to the measured O, Al, and Cr concentration, the calculated fraction of Cr_2O_3 is 20.82 wt.% at Reg-1, and 16.22 wt.% at Reg-2, which is approaching to the formula $(Al_{0.92}Cr_{0.08})_2O_3$ and $(Al_{0.89}Cr_{0.11})_2O_3$, respectively. These results are consistent with oxide solid solution identified by SAED measurement ($(Al_xCr_{1-x})_2O_3$, x=0.85-0.9).
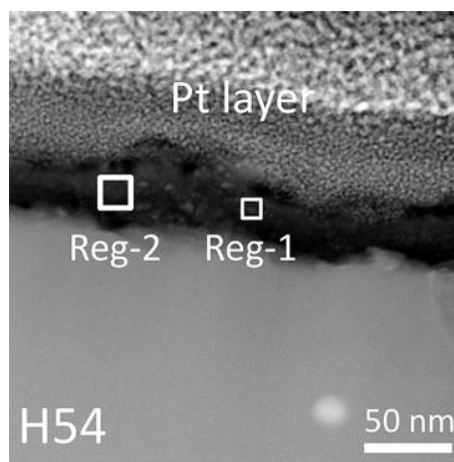
Fig. 14. HAADF-STEM image indicating the areas for EDS analysis of H54 after 2000 h exposure to 10^{-6} wt.% oxygen-containing molten Pb at 600 °C.

Table 4
STEM-EDS standardless quantitative measurements of chemical compositions (wt.%) of regions indicated in Fig. 14.

Region	O(K)	Al(K)	Cr(K)	Fe(K)	Ni(K)
Reg-1	46.91	39.03	13.15	0.88	0.00
Reg-2	53.58	36.40	9.08	0.93	0.00

3.4.2 Alloy H54^{NbY}

A TEM-lamella from alloy H54^{NbY} with Nb and Y addition has been prepared from a magnetite free region by FIB. Fig. 15 summarizes the TEM results obtained from the alloy matrix and oxide scale region. Fig. 15 (a) shows a TEM bright-field image of alloy H54^{NbY}. According to the diffraction pattern shown in Fig. 15 (b), only austenite (f.c.c. phase), in this lamella oriented in <013> zone axis, is identified in the bulk alloy. Fig.15 (c) shows a TEM image of the oxide scale. The corresponding SAED image also shows a ring pattern, which means the formation of nano-crystalline oxides in the surface layer. The phase shown in the SAED can be identified as corundum type $(Al_{0.77}Cr_{0.23})_2O_3$ phase (shown in Fig. 15 (d)). The thickness of the oxide scale is around 100 nm.
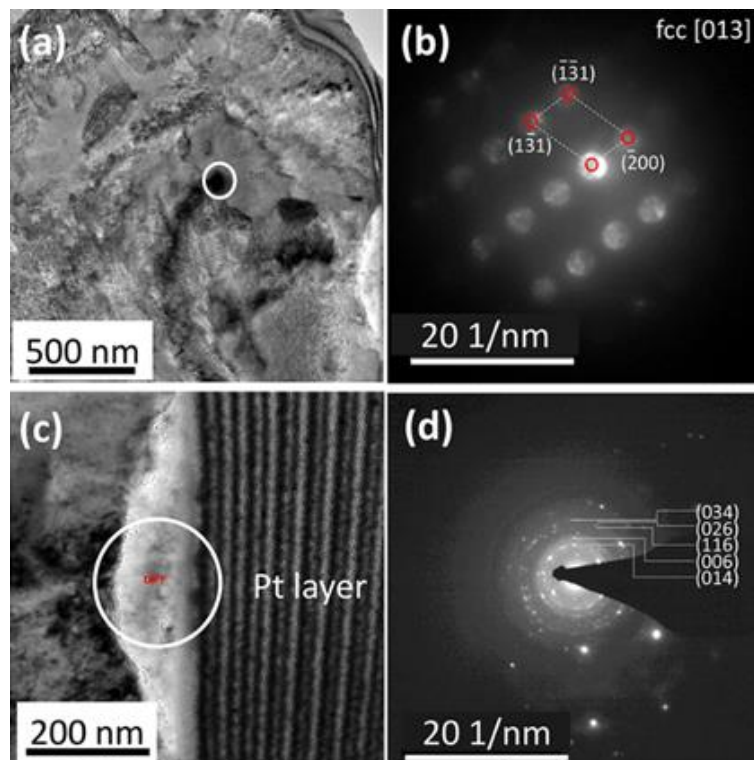
Fig. 15. TEM images of H54^{NbY} alloy after 2000 h exposure to 10^{-6} wt.% oxygen-containing molten Pb at 600 °C. (a) BF overview image, (b) corresponding SAED obtained on bulk alloy, (c) BF image of oxide scale, (d) corresponding SAED of oxide scale.

In addition, drift-corrected STEM-EDS line scans through the oxide scale have been acquired, exemplarily shown in Fig. 16. This line scan shows clearly the elemental distributions in the oxide scale region, with a maximum of the Cr signal at the outer part of the oxide scale and a strong Al signal at the inner part of the scale. Below the oxide scale, a few spots enriched in Al and Ni are detected, which are attributed to the B2-NiAl phase, while other spots show Fe-Nb-enrichment (most

probably Fe$_2$Nb Laves phase). The yellow square in Fig. 16 is the reference area for drift correction during acquisition.
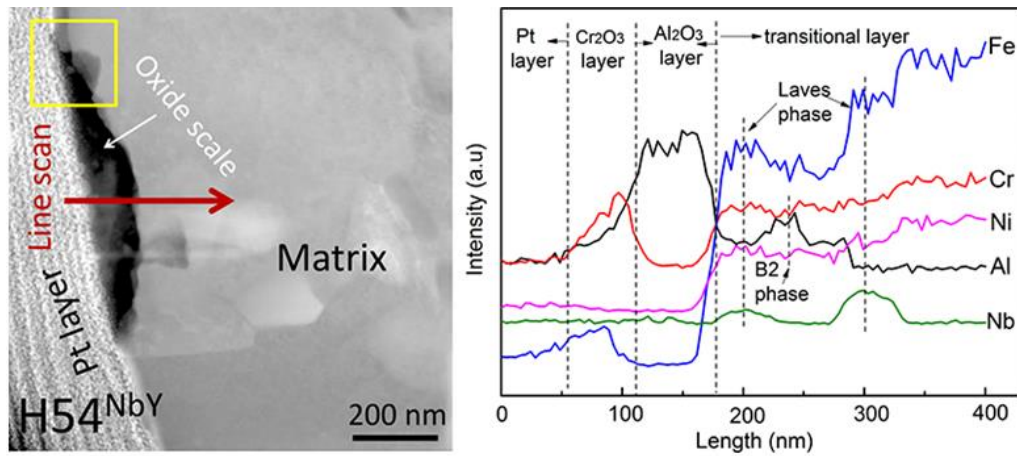
Fig. 16. STEM-HAADF image and STEM-EDS line scan profiles through the cross section of oxide scale formed on H54^{NbY} after 2000 h exposure to 10^{-6} wt.% oxygen-containing molten Pb at 600 °C. The yellow square is used for drift correction.

STEM-HAADF images revealed the formation of precipitates in the alloy matrix. Therefore, drift-corrected EDS elemental mapping has been performed in the bulk alloy (Fig. 17). The orange square in Fig. 17 corresponds to the investigated area; the yellow square is the area used for drift correction. Some areas (300-500 nm) show the enrichment of Al and Ni while Cr and Fe are depleted, indicating the formation of B2-NiAl phase. In addition, some nano sized precipitates (<50 nm) enriched in Nb are observed, which indicates the formation of Fe$_2$Nb Laves phases in the alloy matrix. A few Cr-rich precipitates are also observed in Fig. 17, which may form during the precipitation of B2-NiAl and Fe$_2$Nb Laves compounds.
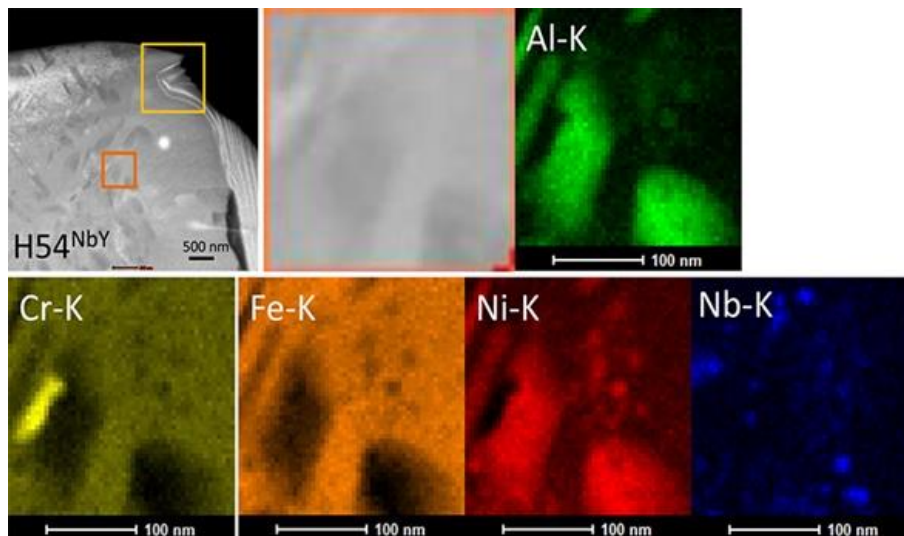
Fig. 17. STEM-HAADF image (upper left), detail of STEM-image (upper middle) and elemental maps of the alloy matrix of H54^{NbY} after 2000 h exposure to 10^{-6} wt.% oxygen-containing molten Pb at 600 °C.

Fig. 18 shows another area of the matrix with STEM-HAADF imaging and the drift-corrected EDS profiles across different precipitates. Two types of precipitates displayed in bright and dark contrast are identified. The bright appearing ones, according to the scan profile, can be attributed to a Nb-rich Laves phase. The dark appearing precipitates, showing signals from both Al and Ni, are the identified B2-NiAl phase. The yellow square in Fig. 18 is the reference area for drift correction during acquisition.
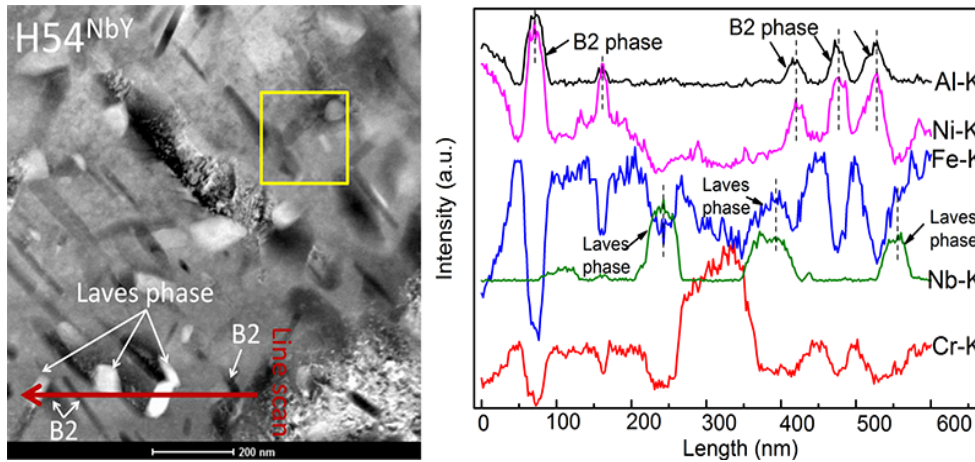
Fig. 18. STEM-HAADF image and STEM-EDS line profiles through precipitates in the alloy matrix of H54[NbY] after 2000 h exposure to 10^{-6} wt.% oxygen-containing molten Pb at 600 °C.

4. Discussion

Fe-Cr-Al-Ni based AFA model alloys, designed for aggressive environment applications, have been investigated with respect to their corrosion behaviour in oxygen-containing molten Pb at 600 °C and 650 °C. Two important observations were made during these experiments: (a) the influence of the minor alloying elements (Y and Nb) on the corrosion properties and phase formation in the alloy matrix is significant and (b) a higher Ni-content in the alloy degrades the formation of a continuous oxide scale at 650 °C and 3550 h.

Compared with the AFA samples H54 and H56 exposed to 600 °C for 1000 h [9], extending the exposure time to 2000 h does not degrade the corrosion resistance of AFA alloys. These results indicate the high stability of alumina-rich oxide scale in aggressive molten Pb environment.

The oxide scale grown on all AFA alloys at 600 °C is mainly $(Al,Cr)_2O_3$ solid solution. The fraction of Cr_2O_3 in $(Al,Cr)_2O_3$ solid solution can be evaluated based on the (104) diffraction peak obtained from XRD [34]. Fig. 19 plots the relationship between the diffraction angle 2θ corresponding to the (104) diffraction peak and the Cr_2O_3 content (in wt%). From this relationship, based on the measured diffraction angle, the Cr_2O_3 content in $(Al,Cr)_2O_3$ solid solution of sample H54 exposed to different conditions is determined. The data related to 550 and 600 °C for 1000 h exposure in molten Pb are taken from a previous publication [9]. They correspond to a Cr_2O_3 content of around 42 wt.% and 34 wt.%, respectively. According to the 2θ peak positions for sample H54 after 2000 h exposure to 600 °C (green triangle in Fig. 19), Cr_2O_3 content is around 16 wt.%. This value fits the results obtained from STEM-EDS analysis of the oxide scale, 16.22-20.82 wt.% Cr_2O_3 measured by STEM-EDS. The shift

of the 2θ peak position indicates that the proportion of alumina in $(Al,Cr)_2O_3$ solid solution increases as exposure temperature or/and time increase.
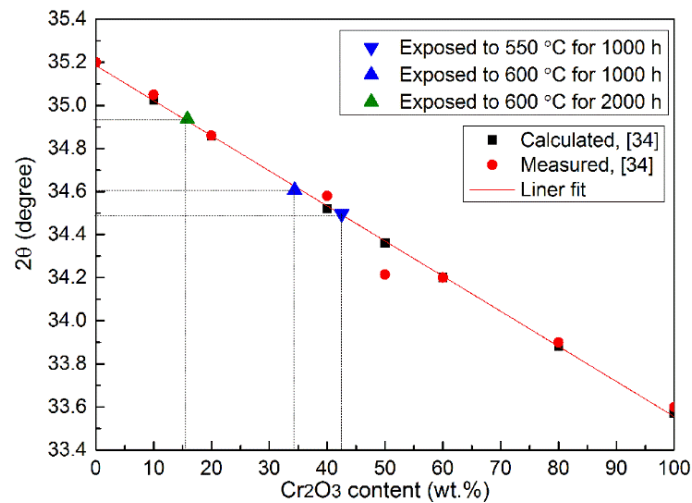
Fig. 19. Cr_2O_3 content (wt.%) in $(Al,Cr)_2O_3$ solid solution of H54 according to (104) diffraction peak obtained by XRD; ■, ●: data obtained from ref [34]; ▼: 2θ = 34.50°, 42.5 wt.% Cr_2O_3; ▲: 2θ = 34.62°, 34.4 wt.% Cr_2O_3; ▲: 2θ = 34.92°, 16.0 wt.% Cr_2O_3.

Increasing the exposure temperature from 600 °C to 650 °C has significant influence on the corrosion behaviour of AFA alloys exposed to oxygen-containing molten Pb. On one hand, the oxidation of AFA H54[NbY] alloy is accelerated at 650 °C, compared with 600 °C, in terms of the formation of a thicker oxide layer (~ 0.35 μm) and a thicker transitional layer (up to 4 μm), depleted in Al and enriched in Ni. On the other hand, the dissolution of Ni in molten Pb increases as the exposure temperature increases [1, 35]. Therefore, alloys H54 and H56, which form protective oxide scales at 600 °C, show dissolution attack at 650 °C. Moreover, the higher Ni content increases the susceptibility to dissolution attack due to the high solubility of Ni in molten Pb [1, 35]. This explains the observation that H54[NbY] (22.9 wt.% Ni) shows corrosion resistance at 650 °C while H56[NbY] (28 wt.% Ni) is affected by dissolution attack.

The $Fe(Cr,Al)_2O_4$ nodules with spinel-type crystalline structure, observed in the oxide scale of the Y-free alloys (H54 and H56) exposed at 600 °C, are a few times thicker than the Al-Cr-based oxide scale, because the growth rate of this oxide is higher than that of $(Al,Cr)_2O_3$. Such nodules of non-protective and fast growing Fe-based oxide might degrade the scale adherence, due to structural and growth stresses, and the heat transfer from the base alloy [10, 36]. By adding yttrium, the oxide scales formed at 600 °C on H54[NbY] and H56[NbY] made from $(Al,Cr)_2O_3$ are uniform in thickness, without spinel-type nodules. This significant change of the oxide scale morphology and composition can be attributed mainly to the yttrium addition, an element that facilitates the selective oxidation of Cr instead of Fe, very important especially during the early, transient stage of the oxidation [37]. Underneath the Cr_2O_3 layer, the oxygen partial pressure drops to a level that favours the selective oxidation of Al and the predominantly inward growth of the Al-based oxide. Hence, Cr_2O_3 serves as a first protective layer, as oxidation retardant and, having a corundum-type structure, as nucleation

centres for α-Al_2O_3 formation. It can be concluded that the yttrium induces a faster development of the protective $(Al,Cr)_2O_3$ scale by promoting the selective oxidation of Cr and Al (to the Fe detriment).

Likewise, with the yttrium addition, the thickness of the transitional layer (TL) observed underneath the oxide scale decreases, since the transport mechanism through the oxide scale changes from mixed cation and anion diffusions as in case of the H54 alloy (Fig. 7) to predominantly anion (oxygen) inward transport as in the H54[NbY] case (Fig. 9) [38].

Besides yttrium, the influence on the corrosion behaviour of the niobium addition is also considered. According to literature, minor addition of niobium to alumina-forming austenitic steels enhances the concentration of Cr in the austenitic phase and increases the volume fraction of B2-NiAl phase [39]. Both effects, visible in the transitional layer of H54[NbY] (Fig. 17), namely the formation of Cr-rich and of B2-NiAl precipitates adjacent to Fe_2Nb grains, are important for protective alumina scale formation, given their proximity to the alloy surface. The increased Cr level supports the formation of a protective Cr_2O_3 as fast as possible, while B2-NiAl precipitates provide an Al reservoir for the alumina scale formation underneath.

The beneficial Nb addition on the precipitation of B2-NiAl compound during the corrosion tests is more obvious at 600 °C. After 2000 h, the H54 and H56 alloys show no visible change in the bulk microstructure, whereas the alloys containing Nb (H54[NbY] and H56[NbY]) exhibit fine grains of the B2-NiAl phase and Fe_2Nb phase precipitated in the austenite matrix (Fig. 18). However, after corrosion tests at higher temperature (650 °C) and longer time exposure (3550 h), the precipitation of B2-NiAl is observed also in the alloys without Nb addition (Fig. 3c).

The co-precipitation of B2-NiAl and Fe_2Nb Laves phases has been observed previously in AFA alloys microstructure [20, 26, 39]. One possible explanation is that the precipitation of Fe_2Nb Laves phase leads to the occurrence of Fe-depleted regions, in which the formation of B2-NiAl phase and of Cr-rich ferrite is triggered in adjacent location, at lower temperature than in the Nb-free alloys.

At 650 °C, the positive influence of Y and Nb minor additions on the corrosion behaviour was also observed. H54 shows dissolution attack, whereas the H54[NbY] alloy is protected by a $(Al,Cr)_2O_3$ scale. The depletion of B2-NiAl precipitates in the transitional layer (Fig. 12) is the proof that these precipitates serve as reservoir for the alumina scale formation and growth. Ni and Fe enrichments in the transitional layer are underlining the efficiency of the formed oxide scale as a diffusion barrier for these elements. Neither H56[NbY] nor its precursor H56, both with higher Ni concentration, show the capacity to form/maintain a protective alumina scale, displaying a selective leaching of Ni. In this case the most probable explanation resides in an inadequate Ni/CrAl ratio in the alloy composition. A slight increase ($\sim$ 1-2 wt.%) of Cr, or preferable of Nb concentration could drive the formation of a stable, protective $(Al,Cr)_2O_3$ scale on AFA model alloys with 28 wt% Ni.

5. Conclusion

This work is a comprehensive study of the corrosion behaviour of alumina-forming austenitic model alloys exposed to oxygen-containing molten Pb at 600 °C and 650 °C. Based on the results, the main conclusions are:

(a) AFA model alloys with the composition formula Fe-(15.2-16.6)Cr-(3.8-4.3)Al-(22.9-28.5)Ni (wt.%) have shown corrosion resistance to oxygen containing molten Pb at 600 °C. By increasing the exposure temperature to 650 °C, the only alloy that forms a protective oxide scale is the alloy with lower Ni content (~23 wt.%) and minor additions of Nb and Y. A higher Ni content of ~28 wt.% increases the susceptibility to corrosion attack at 650 °C.

(b) Yttrium minor addition brings a significant benefit to the corrosion behaviour of AFA model alloys, since it facilitates the selective oxidation of Cr and Al to the Fe detriment and impedes Fe(Cr,Al)$_2$O$_4$ formation.

(c) Niobium minor addition increases the Cr availability in austenite, supports the earlier Cr$_2$O$_3$ formation, and triggers/enhances the precipitation of B2-NiAl phase, which serves as Al reservoir for the alumina scale formation.

Data availability

The raw/processed data required to reproduce these findings cannot be shared at this time due to technical or time limitations.

The datasets obtained during the current study are available from the corresponding author on reasonable request.

Acknowledgment

References

[1] C. Fazio, V.P. Sobolev, A. Aerts, S. Gavrilov, K. Lambrinou, P. Schuurmans, A. Gessi, P. Agostini, A. Ciampichetti, L. Martinelli, S. Gosse, Handbook on lead-bismuth eutectic alloy and lead properties, materials compatibility, thermal-hydraulics and technologies-2015 edition (No. NEA--7268), Organisation for Economic Co-Operation and Development.2015.

[2] V. Sobolev, Database of thermophysical properties of liquid metal coolants for GEN-IV, Scientific Report SCIENTIFIC REPORT SCK•CEN-BLG-1069, Mol Belgium, ISSN 1379-2407, 2011.

[3] V.P. Sobolev, P. Schuurmans, G. Benamati, Thermodynamic properties and equation of state of liquid lead and lead–bismuth eutectic, J. Nucl. Mater. 376 (2008) 358-362, https://doi.org/10.1016/j.jnucmat.2008.02.030.

[4] Z. Su'ud, H. Sekimoto, Design and safety aspect of lead and lead-bismuth cooled long-life small safe fast reactors for various fore configurations, J. Nucl. Sci. Technol. 32 (1995) 834-845,

https://doi.org/10.1080/18811248.1995.9731785.

[5] F. Roelofs, B. de Jager, A. Class, H. Jeanmart, P. Schuurmans, A. Ciampichetti, G. Gerbeth, R. Stieglitz, C. Fazio, European research on HLM thermal hydraulics for ADS applications, J. Nucl. Mater. 376 (2008) 401-404, https://doi.org/10.1016/j.jnucmat.2008.02.014.

[6] D. Frazer, E. Stergar, C. Cionea, P. Hosemann, Liquid metal as heat transport fluid for thermal solar power applications, Energy Procedia 49 (2014) 627-636, https://doi.org/10.1016/j.egypro.2014.03.068.

[7] J. Pacio, T. Wetzel, Assessment of liquid metal technology status and research paths for their use as efficient heat transfer fluids in solar central receiver systems, Sol. Energy 93 (2013) 11-22, https://doi.org/10.1016/j.solener.2013.03.025.

[8] H. Kim, D. Boysen, J. Newhouse, B. Spatocco, B. Chung, P. Burke, D. Bradwell, K. Jiang, A. Tomaszowska, K. Wang, W. Wei, L. Ortiz, S. Barriga, S. Poizeau, D. Sadoway, Liquid metal batteries: past, present, and future, Chem. Rev. 113 (2013) 2075-2099, https://doi.org/10.1021/cr300205k.

[9] H. Shi, A. Jianu, A. Weisenburger, C. Tang, A. Heinzel, R. Fetzer, F. Lang, R. Stieglitz, G. Müller, Corrosion resistance and microstructural stability of austenitic Fe–Cr–Al–Ni model alloys exposed to oxygen-containing molten lead, J. Nucl. Mater. 524 (2019) 177-190, https://doi.org/10.1016/j.jnucmat.2019.06.043.

[10] H. Shi, Alumina forming alloys (steels, high entropy materials) for the mitigation of compatibility issues with liquid metals and steam in energy related, high-temperature applications, Karlsruher Institut für Technologie (KIT), Karlsruhe, 2020, DOI: 10.5445/IR/1000105453.

[11] K. Lambrinou, V. Koch, G. Coen, J. van den Bosch, C. Schroer, Corrosion scales on various steels after exposure to liquid lead-bismuth eutectic, J. Nucl. Mater. 450 (2014) 244-255, https://doi.org/10.1016/j.jnucmat.2013.09.034.

[12] G. Müller, A. Heinzel, J. Konys, G. Schumacher, A. Weisenburger, F. Zimmermann, V. Engelo, A. Rusanov, V. Markov, Behaviour of steels in flowing liquid PbBi eutectic alloy at 420–600 °C after 4000–7200 h, J. Nucl. Mater. 335 (2004) 163-168, https://doi.org/10.1016/j.jnucmat.2004.07.010.

[13] C. Schroer, O. Wedemeyer, J. Novotny, A. Skrypnik, J. Konys, Selective leaching of nickel and chromium from Type 316 austenitic steel in oxygen-containing lead–bismuth eutectic (LBE), Corros. Sci. 84 (2014) 113-124, https://doi.org/10.1016/j.corsci.2014.03.016.

[14] V. Tsisar, C. Schroer, O. Wedemeyer, A. Skrypnik, J. Konys, Long-term corrosion of austenitic steels in flowing LBE at 400 °C and 10−7 mass% dissolved oxygen in comparison with 450 and 550 °C, J. Nucl. Mater. 468 (2016) 305-312, https://doi.org/10.1016/j.jnucmat.2015.09.027.

[15] J.R. Weeks, Lead, bismuth, tin and their alloys as nuclear coolant, Nucl. Eng. Des. 15 (1971) 363-372, https://doi.org/10.1016/0029-5493(71)90075-6.

[16] K. Lambrinou, E. Charalampopoulou, T. Van der Donck, R. Delville, D. Schryvers, Dissolution corrosion of 316L austenitic stainless steels in contact with static liquid lead-bismuth eutectic (LBE) at 500 °C, J. Nucl. Mater. 490 (2017) 9-27, https://doi.org/10.1016/j.jnucmat.2017.04.004.

[17] M.P. Brady, Y. Yamamoto, M.L. Santella, P.J. Maziasz, B.A. Pint, C.T. Liu, Z.P. Lu, H. Bei, The development of alumina-forming austenitic stainless steels for high-temperature structural use, JOM 60 (2008) 12, https://doi.org/10.1007/s11837-008-0083-2.

[18] Y. Yamamoto, M.P. Brady, Z.P. Lu, P.J. Maziasz, C.T. Liu, B.A. Pint, K.L. More, H.M. Meyer, E.A. Payzant, Creep-resistant, Al_2O_3-forming austenitic stainless steels, Science 316 (2007) 433-436, 10.1126/science.1137711.

[19] B. Hu, I. Baker, The effect of thermo-mechanical treatment on the high temperature tensile behaviour of an alumina-forming austenitic steel, Mater. Sci. Eng. A 651 (2016) 795-804, https://doi.org/10.1016/j.msea.2015.11.036.

[20] L.Z. Chen, M. Wang, Q. Wang, Y. Gao, H. Dong, H.Y. Che, Z.J. Zhou, Microstructure and mechanical property evolution of an AFA alloy with simple composition design during ageing at 700 °C, Mater. Sci. Eng. A 779 (2020) 139157, https://doi.org/10.1016/j.msea.2020.139157.

[21] H. Shi, C. Tang, A. Jianu, R. Fetzer, A. Weisenburger, M. Steinbrueck, M. Grosse, R. Stieglitz, G. Müller, Oxidation behaviour and microstructure evolution of alumina-forming austenitic & high entropy alloys in steam environment at 1200° C. Corros. Sci. 170 (2020) 108654, https://doi.org/10.1016/j.corsci.2020.108654.

[22] Y. Yamamoto, M.P. Brady, M.L. Santella, H. Bei, P.J. Maziasz, A.B. Pint, Overview of Strategies for High-Temperature Creep and Oxidation Resistance of Alumina-Forming Austenitic Stainless Steels, Metall Mater Trans A. 42 (2011) 922-931, https://doi.org/10.1007/s11661-010-0295-2.

[23] Y. Yamamoto, G. Muralidharan, M.P. Brady, Development of L12-ordered Ni3(Al,Ti)-strengthened alumina-forming austenitic stainless steel alloys, Scr. Mater. 69 (2013) 816-819, https://doi.org/10.1016/j.scriptamat.2013.09.005.

[24] R. Bousquet, D. Fayeulle, E. Bruyere, F. Bertrand, Effects of Yttrium on the Oxidation Behaviour of Low Sulfur Content Fe–Cr–Al Alloys for Heat Resistant Wires, Oxid. Met. 80 (2013) 13–24, https://doi.org/10.1007/s11085-013-9403-1.

[25] B. A. Pint, Optimization of Reactive-Element Additions to Improve Oxidation Performance of Alumina-Forming Alloys, J Am Ceram Soc, 86 (2004) 686-95, https://doi.org/10.1111/j.1151-2916.2003.tb03358.x.

[26] H. Meng, J. Wang, L. Wang, X. Fang, N. Dong, C. Zhang, P. Han, The precipitation control in aged alumina-forming austenitic stainless steels Fe-15Cr-25Ni-3Al-NbWCu by W addition and its effect on the mechanical properties, Mater Charact. 163 (2020) 110233, https://doi.org/10.1016/j.matchar.2020.110233.

[27] Y. Yamamoto, M.L. Santella, C.T. Liu, N.D. Evans, P.J. Maziasz, M.P. Brady, Evaluation of Mn substitution for Ni in alumina-forming austenitic stainless steels, Mater. Sci. Eng. A. 524 (2009) 176-185, https://doi.org/10.1016/j.msea.2009.06.043.

[28] J. Ejenstam, P. Szakalos, Long term corrosion resistance of alumina forming austenitic stainless steels in liquid lead, J. Nucl. Mater. 461 (2015) 164-170, https://doi.org/10.1016/j.jnucmat.2015.03.011.

[29] W. Ding, H. Shi, A. Jianu, Y. Xiu, A. Bonk, A. Weisenburger, T. Bauer, Molten chloride salts for next generation concentrated solar power plants: mitigation strategies against corrosion of structural materials, Sol. Energy Mater. Sol. Cells 193 (2019) 298–313, https://doi.org/10.1016/j.solmat.2018.12.020.

[30] G. Muller, G. Schumacher, F. Zimmermann, Investigation on oxygen controlled liquid lead corrosion of surface treated steels, J. Nucl. Mater. 278 (2000) 85-95, https://doi.org/10.1016/S0022-3115(99)00211-1.

[31] C. Schroer, Guidelines for corrosion testing in liquid metals (Pb, LBE), MATTER project, 2015, retrieved on 01.06.2020, www.eera-jpnm.eu/filesharer/documents/_Euratom_Projects/Past%20projects/MATTER%20public%20deliverables/Deliverable%20D3.4%20MATTER.pdf.

[32] A. Ul-Hamid, A Beginners' Guide to Scanning Electron Microscopy, Springer, Cham, 2018, ISBN: 978-3-319-98482-7.

[33] A. Weisenburger, A. Jianu, S. Doyle, M. Bruns, R. Fetzer, A. Heinzel, M. DelGiacco, W. An, G. Müller, Oxide scales formed on Fe–Cr–Al-based model alloys exposed to oxygen containing molten lead, J. Nucl.Mater. 437(2013) 282-292. https://doi.org/10.1016/j.jnucmat.2013.02.044.

[34] P. Zhao, H. Zhao, J. Yu, H. Zhang, H. Gao, Q. Chen, Crystal structure and properties of Al_2O_3-Cr_2O_3 solid solutions with different Cr_2O_3 contents, Ceram. Int. 44 (2018) 1356-1361, https://doi.org/10.1016/j.ceramint.2017.08.195.

[35] J. Zhang, N. Li, Review of the studies on fundamental issues in LBE corrosion, J. Nucl.Mater. 373 (2008) 351-377. https://doi.org/10.1016/j.jnucmat.2007.06.019.

[36] A. Jianu, R. Fetzer, A. Weisenburger, S. Doyle, M. Bruns, A. Heinzel, P. Hosemann, G. Mueller, Stability domain of alumina thermally grown on FeCrAl-based model alloys and modified surface layers exposed to oxygen containing molten Pb, J. Nucl. Mater. 470 (2016) 68-75. https://doi.org/10.1016/j.jnucmat.2015.12.009.

[37] F.H. Stott, G.C. Wood, J. Stringer, The influence of alloying elements on the development and maintenance of protective scales, Oxid. Met. 44 (1995) 113-145, https://doi.org/10.1007/BF01046725.

[38] B.A. Pint, J.A. Martin, L.W. Hobbs, 18O/SIMS characterization of the growth mechanism of doped and undoped α-Al_2O_3, Oxid. Met. 39 (1993) 167-195, https://doi.org/10.1007/BF00665610.

[39] M.P. Brady, Y. Yamamoto, M.L. Santella, L.R. Walker, Composition, microstructure, and water vapor effects on internal/external oxidation of alumina-forming austenitic stainless steels, Oxid. Met. 72 (2009) 311. https://doi.org/10.1007/s11085-009-9161-2.